Influence of carrier trapping on radiation detection properties in CVD grown 4H-SiC epitaxial layers with varying thickness up to 250 µm

Joshua W. Kleppinger, Sandeep K. Chaudhuri, OmerFaruk Karadavut, Ritwik Nag, and Krishna C. Mandal*

*Department of Electrical Engineering, University of South Carolina, Columbia, SC 29208, USA

Abstract: Low doped n-type 4H-SiC epitaxial layers of thickness 50, 150, and 250 µm grown by hot wall chemical vapor deposition were used to fabricate Ni/4H-SiC Schottky radiation detectors. The epitaxial layers were grown on the (0001) face of highly conductive bulk 4H-SiC substrates 8° offcut towards the $\langle 11\bar{2}0 \rangle$ direction. The 50, 150, and 250 µm thick epilayer detectors, under optimized settings, showed energy resolutions of 2.0%, 0.78%, and 0.63%, respectively for 5.48 MeV alpha particles. Deep level transient spectroscopy studies showed that the observed variation in the detector resolution is linked to the defect parameters in the devices. Least-squares fitting of the bias dependence of the charge collection efficiency according to a drift-diffusion model, revealed minority carrier diffusion lengths of 16, 10, and 9.2 µm, respectively, implying that the detectors are not limited by minority carrier trapping. The detector performance was observed to be primarily dependent on the concentration and capture cross-sections of the lifetime killing electron traps $Z_{1/2}$ and $EH_{6/7}$.

Keywords: B2. 4H-SiC, A3. Epitaxial layers, B3. Radiation detectors, A1. Charge collection efficiency, and A1. Deep level transient spectroscopy (DLTS)

1. Introduction

Electronic devices based on group IV compound semiconductor 4H-SiC has been widely used in harsh environments with high temperatures or high radiation backgrounds [1-8]. With its wide-bandgap of 3.27 eV and high thermal conductivity of 4.9 W/cm^2, 4H-SiC devices can operate continuously at temperatures up 1000 ºC [9]. Furthermore, due to the strong triple covalent bonding between the Si and C atoms, 4H-SiC has high atomic displacement thresholds (19 eV for C and 42 eV for Si) [10] making it radiation hard. Additionally, it has excellent charge transport properties such as a high electron saturation drift velocity of 2.0×10^7 cm/s and high breakdown electric field of 2.0 MV/cm. Such unique combination of physical properties allows applications of 4H-SiC radiation detectors in nuclear waste characterization, nuclear core reactor monitoring, space missions, and high energy physics experiments [11-13].

One of the key limitations of 4H-SiC is the low atomic number of its constituent atoms which make it nearly blind to even low energy gamma rays. This can be mitigated by using semi-insulating (SI) bulk 4H-SiC however, SI bulk 4H-SiC has too many defects for effective charge collection [14-16]. Defects in the crystalline structure can capture charge carriers affecting the charge carrier transport properties adversely [17-18]. An alternative approach is to fabricate Schottky barrier radiation detectors on high quality, low doped ($\leq 10^{14}$ cm^{-3}) 4H-SiC epitaxial layers with low concentrations of lifetime limiting deep levels $Z_{1/2}$ and $EH_{6/7}$ [19, 20], basal plane dislocations (BPD), and micropipes (MP). BPDs are defects that propagate upward from the substrate to the epilayer and can introduce stacking faults which degrade device performance. MPs are a type of screw dislocation originating from the substrate and are thought to be the primary source of device failure in SiC devices. BPDs can be eliminated through KOH etching or converted into benign threading edge dislocations—a process that is facilitated when the growth is slightly off-axis or at higher C/Si ratios [21-24]. Micropipes, on the contrary, are more likely to close at lower C/Si ratios preventing them from acting as leakage current pathways [24]. The lifetime limiting deep levels appear at lower concentrations at high C/Si ratios and lower temperatures [24, 25]. While the

relationship between deep levels and radiation detector performance has been studied in the past [4, 26-28], there have not been any comparative studies on epilayers of varying thickness up to 250 µm.

In this article, we report on the characterization of Ni/n-4H-SiC Schottky barrier radiation detectors fabricated on hot-wall CVD grown 4H-SiC epitaxial layers of thicknesses 50, 150, and 250 µm. The impact of both minority and majority carrier trapping centers on the radiation detection performance are investigated from the bias dependence of the radiation response and capacitance-mode deep level transient spectroscopy (DLTS).

2. Experimental Methods

2.1 Device Fabrication

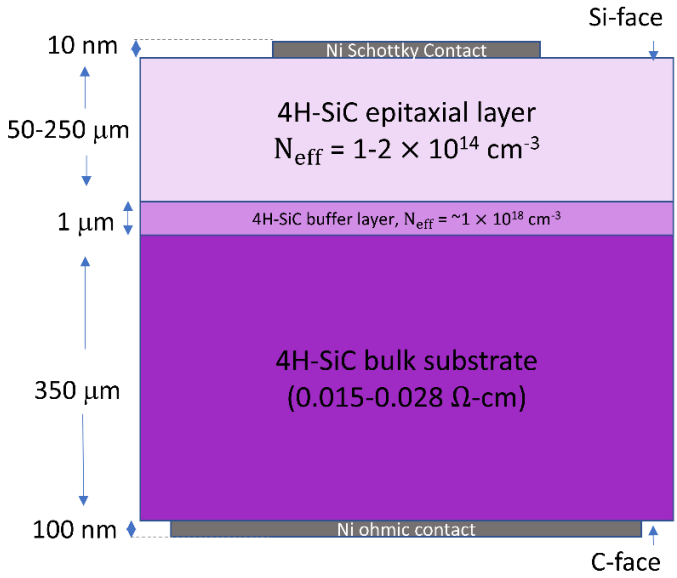

Figure 1. Cross-sectional schematic of the detectors fabricated using 50, 150, and 250 µm thick 4H-SiC epitaxial layers.

4H-SiC epitaxial layers of thicknesses 50, 150, and 250 µm were grown via hot wall chemical vapor deposition (CVD) on the (0001) surface of a low resistivity (0.015-0.028 Ω-cm) 100 mm diameter, 350 µm thick bulk 4H-SiC substrate offcut by 8° and oriented towards the $\langle 11\bar{2}0 \rangle$ direction. The 100 mm diameter parent wafers were diced into 8 × 8 mm^2 samples and cleaned for metal contact deposition using the Radio Corporation of America (RCA) cleaning method [29]. Metal contacts were deposited by DC sputtering nickel onto both the epilayer (Si-face) and bulk (C-face) surfaces of the individual samples using a Quorum Q150T sputtering unit. For the radiation detection measurements, the circular top contact area (3.9 mm diameter) acts as the detector window. As such, the thickness of the top contact should be as thin as possible (~10 nm) showing a rectifying behavior. The bottom contact is ~36 mm^2 square shaped and relatively thicker (> 100 nm) to ensure the formation of the Ohmic contact. A schematic of the detector structure is shown in Fig. 1.

2.2 Detector Characterization

The properties of the junction between the metal and the epitaxial layer and the net donor concentrations were determined from the current-voltage (*I-V*) and capacitance-voltage (*C-V*) characteristics of the detectors. The *I-V* measurements were recorded using a Keithley 237 source-measure unit with the detector mounted on a PCB inside an electromagnetic interference (EMI) shielded electronic box connected via a low-noise triaxial cable. *C-V* measurements were conducted with a 1 MHz capacitance meter built-in to a SULA DDS-12 DLTS system.

Radiation detection properties were evaluated from their response to alpha particles generated from the decay of a 0.9 μCi ^{241}Am calibration source. The photoinduced current generated in the detector from the alpha particles was fed into and integrated by a CR110 charge sensitive preamplifier producing an output signal directly proportional to the charge collected by the detector. The signal was shaped and filtered into a semi-gaussian form by an ORTEC 572 shaping amplifier. The amplitude of the shaped gaussian was converted into a 13-bit integer value via a Canberra Multiport II multichannel analyzer and recorded into a histogram showing how often various pulse heights are collected. This histogram is often referred to as the pulse-height spectrum (PHS). The resolution of each detector was expressed as the ratio of the full width at half maximum of the dominant alpha peak in the spectrum to its centroid channel number.

2.3 Defect Characterization

The electron trap activation energies, cross-sections, and concentrations were determined from capacitance mode deep-level transient spectroscopy measurements performed using a SULA DDS-12 DLTS comprised of a 1 MHz capacitance meter, a pulse generator, a correlator module, and a LabVIEW based data acquisition and analysis program. The system allows for up to twelve rate window ($\Delta\tau$) settings with the initial time set to $\Delta\tau/4.3$ msec. The sample was mounted on the sample stage of a Janis VPF 800 liquid nitrogen cooled cryostat which was connected to the pulse generator output and capacitance meter input of the DLTS system via low noise BNC cables. The temperature of the sample stage was controlled automatically by a Lakeshore LS335 temperature controller.

3. Results/Discussion

3.1 Electrical Characterization

As presented in Figs. 2(a) and (b), all the three devices show rectifying characteristics consistent with the behavior of Schottky barrier diodes. From the forward bias characteristics, the properties of the junction can be evaluated using the thermionic emission model [30, 31] given by,

$$J = A^{*}T^{2}\exp\left(-\frac{q\Phi_B}{kT}\right)\left[\exp\left(\frac{qV}{nkT}\right)-1\right] \quad (1)$$

where A^{*} is the Richardson constant of the material (~146 A cm^{-2} K^{-2} in 4H-SiC), T is temperature, q is the elementary charge of an electron, k is Boltzmann's constant, Φ_B is the effective barrier height of the junction, n is the ideality factor, and V is the applied bias. The factor outside the brackets is collectively called the reverse saturation current density J_s which can be extracted from the y-intercept of the linear fit of $\ln J$ vs. V plots. The effective barrier height is calculated form the obtained J_s value provided the Richardson constant for the semiconductor and the device temperature is known. Additionally, the ideality factor n can be extracted from the slope of the $\ln J$ vs. V plots. Using the above-mentioned method, the barrier heights were calculated to be 1.43, 1.55, and 1.46 eV with the diode ideality factors of 1.30, 1.56, and 1.14 for the detectors fabricated on 50, 150, and 250 μm epilayers, respectively. While 150 μm had the largest effective barrier height, it also had the largest ideality factor of the three detectors

indicating significant spatial variation in the Schottky barrier height. In Schottky barrier radiation detectors, the top metal contact acts as the window for the incident radiation, and thus larger contact areas can improve detection efficiency for a given source-detector gap. The drawback of having larger contact area is that it increases the probability of spatial variation in surface barrier and dislocations resulting in the increase of ideality factor and form low barrier patches [32, 33]. For all the three devices, the reverse bias leakage current showed linearity with the electric field indicating drift-diffusion behavior [31]. For the 50 and 150 µm detectors, leakage current remained less than 1 nA/cm^{-2} up to -100 V [78 kV/cm] while the 250 µm detector exhibited reverse current densities less than 2 nA/cm^{2} up to reverse bias as high as -800 V (280 kV/cm). It should be noted that the region of the forward bias characteristics to the left of the linear region for the 50 and 150 µm detectors implied the existence of either a shunting pathway or low barrier patch which would result in the increased leakage current observed under reverse bias for the two detectors compared to the 250 µm detector [5, 34].

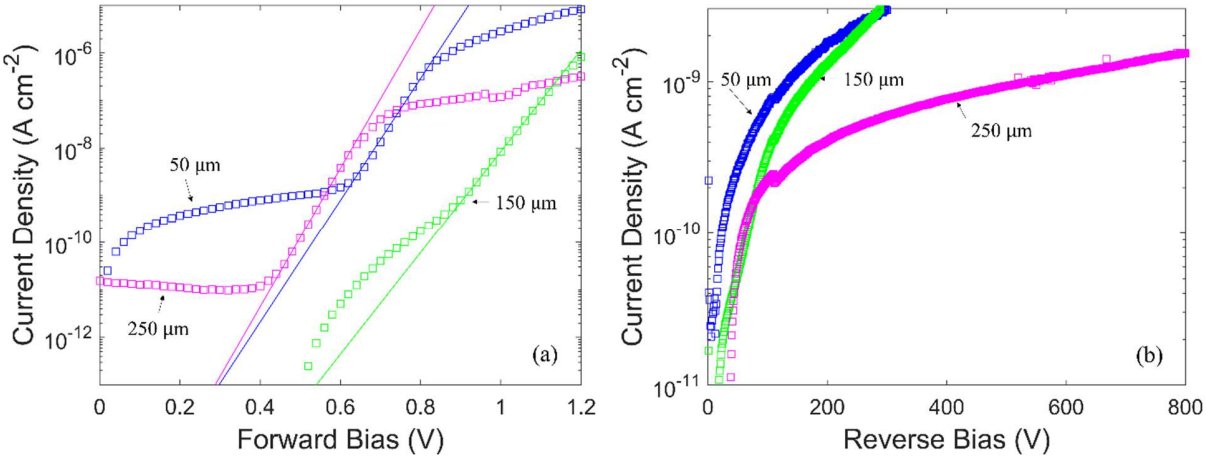

Figure 2. Forward (a) and reverse (b) bias current-voltage characteristics for the detectors fabricated on the 50, 150, and 250 µm epitaxial layers. The solid lines in (a) represent the fit to the linear region of the forward bias characteristics.

From the $1/C^2$ vs. V plot (Mott-Schottky) in Fig. 3, the built-in voltage V_{bi} and the effective carrier concentration can be determined from the linear fit from the following equation,

$$1/C^2 = \frac{2}{A^2 q \epsilon N_{eff}}[V_{bi} - V], \tag{2}$$

where ϵ is the dielectric permittivity of the material (8.5 × 10^{-13} in 4H-SiC) and N_{eff} is the net donor concentration. From the fitted model, the net donor concentrations were between 1.6-1.8 × 10^{14} cm^{-3} for all three detectors. For 50 µm, the built-in voltage was 1.68 V which corresponds to a barrier height of 1.98 eV after adjusting for the bulk fermi energy. This value is higher than the effective barrier extracted from the *I-V* because the *C-V* barrier corresponds to the linear average of the barrier height over the entire surface area whereas the *I-V* barrier represents a temperature-dependent effective value resulting from current preferring to pass through the low barrier regions. The 150 and 250 µm detectors had built-in potentials of 2.60 and 4.56 V, respectively. It's possible that due to the low thickness of the nickel contact, the contact is not rigid enough to accurately measure the built-in voltage. Using the full depletion approximation of Poisson's equation, the bias which will fully deplete the epitaxial layer of each detector can be described by

$$V_{FD} = V_{bi} - \frac{qN_{eff}}{2\epsilon} x_{epi}^2. \quad (3)$$

Here, x_{epi} is the thickness of the epilayer. Using Eq. 3, it has been calculated that full depletion will be achieved at 380 V [150 kV/cm], 3.3 kV [450 kV/cm], and 10 kV [810 kV/cm] for 50, 150, and 250 µm, respectively.

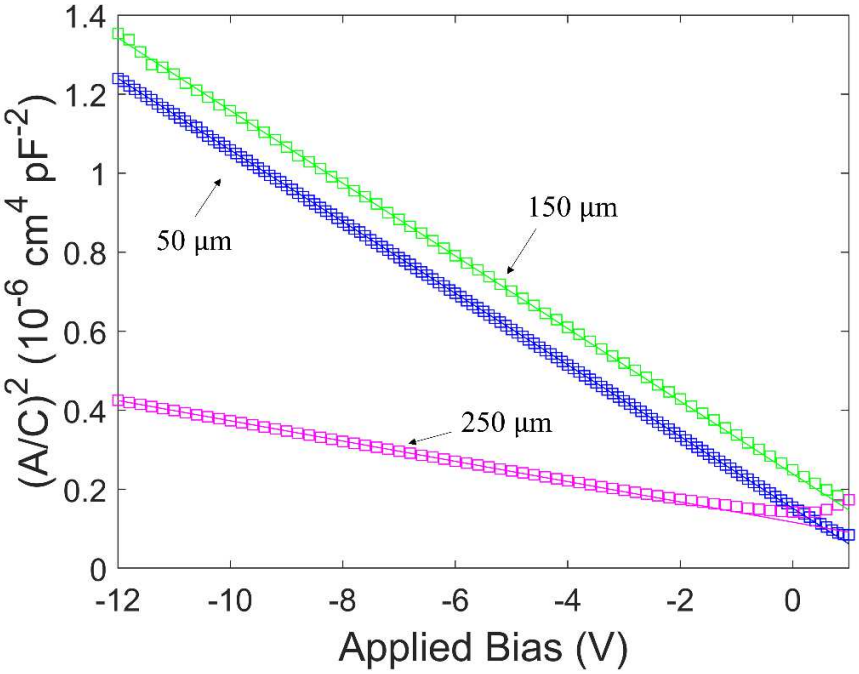

Figure 3. Mott-Schottky plot of detectors fabricated on the 50, 150, and 250 µm epitaxial layers. The solid lines are the linear fits to Eq. 3.

3.2 Radiation Detection Measurements

The best spectrum for each of the three detectors is displayed in Fig. 4 (a)-(c) which had resolutions of 2.0%, 0.78%, and 0.63% for 50, 150, and 250 µm, respectively for the 5486 keV peak. Only the 250 µm detector was able to resolve the 5388 keV and 5443 keV peaks present in the ^{241}Am alpha spectrum. For radiation detectors, the most important properties of the epitaxial layer limiting the device performance are the electron and hole trapping lifetimes τ_n and τ_p which can be used to describe how quickly photoinduced charges are collected vs. how quickly they get trapped and recombine. For electrons and holes generated at a point x_i, this can be described by the single point Hecht equation [35] for charge collected given below,

$$Q_n(x_i) \approx q\frac{\tau_n v_{s,n}}{x_d}\left[1 - \exp\left(-\frac{x_d - x_i}{\tau_n v_{s,n}}\right)\right], \quad (4a)$$

$$Q_p(x_i) \approx q\frac{\mu_p \tau_p \langle E\rangle}{x_d}\left[1 - \exp\left(-\frac{x_i}{\mu_p \tau_p \langle E\rangle}\right)\right], \quad (4b)$$

where $v_{s,n}$ is the electron saturation drift velocity, x_d is the depletion width, and μ_p is the hole mobility. Due to the high electron mobility and strong internal field of the depletion region, electron drift velocity is

assumed to be saturated. Essentially the higher the trapping lifetimes, the more charge is collected and the higher the resolution of the detector.

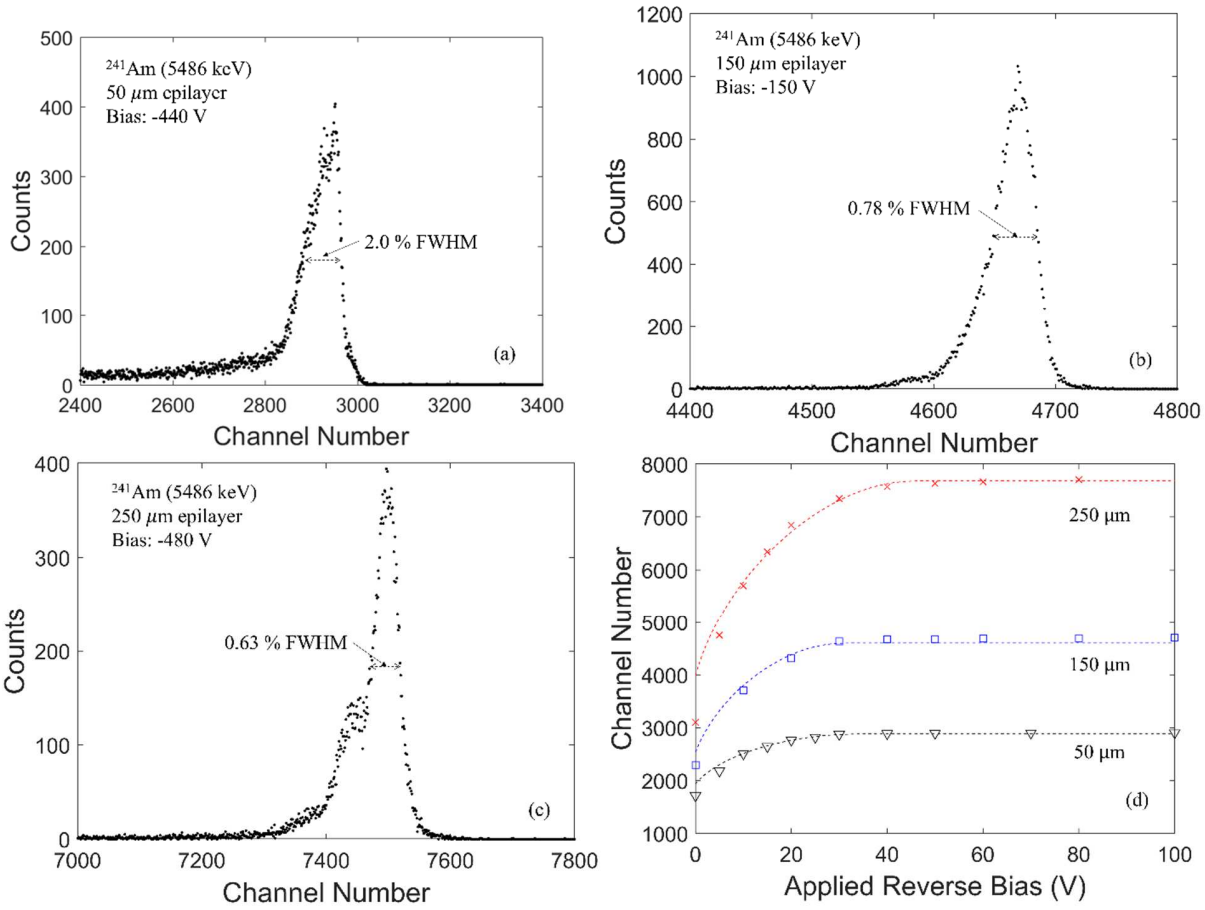

Figure 4. The pulse height spectra at the bias which offered the best resolution for each of the detectors fabricated on 50 (a), 150 (b), and 250 µm (c) 4H-SiC epitaxial layers, and (d) the charge collected as a function of reverse bias fitted to the drift-diffusion model for each of the detectors fabricated on 50, 150, and 250 µm epitaxial layers. The y-axis is given in channel number to make the three curve more distinct.

Unfortunately, charged radiation generates a continuum of electron-hole pairs making evaluating the trapping lifetimes via Eq. 4 nearly impossible. For holes, an alternative approach would be to evaluate each detectors' minority carrier diffusion length L_d which is proportional to square root of τ_p. This can be achieved by fitting the charge collected to the drift-diffusion model [36, 37]. This model states that charge generated within the depletion width will immediately drift with the electric field and induce a charge on the electrodes whereas holes generated in the neutral region must first diffuse into the depletion width and is given by,

$$Q_{total} = \int_0^{x_d} \left(\frac{dQ}{dx}\right) dx + \int_{x_d}^{x_r} \left(\frac{dQ}{dx}\right) \exp\left[-\frac{x - x_d}{L_d}\right] dx\,. \tag{5}$$

Here, dQ/dx is the amount of charge generated per unit length which is directly proportional to the instantaneous stopping power of the alpha particle and x_r is the maximum range of the alpha particle simulated in SRIM. For ^{241}Am impacting with 4H-SiC, x_r is 18.22 µm. Fig. 4 (d) shows the variation of

alpha peak channel number as a function of the applied bias for each of the detectors. From the fitted models, the minority carrier diffusion lengths were calculated to be 16, 10, and 9.2 µm for the detectors fabricated on 50, 150, and 250 µm, respectively which implies that the resolution is not limited by hole trapping. Based on the stopping power (Bragg) curve for ^{241}Am in 4H-SiC, most of the electron-hole pairs are generated towards the end of the particle's path, and as a result, most of the charge transport is hole transport when the depletion width is less than or equal to the particle range. However, as the depletion width increases, electrons must travel further to the anode whereas the hole transit distance remains the same. Thus, the charge collected eventually switches to predominantly electron induced as the applied bias increases minimizing the effect of hole trapping on the detector resolution. A summary of the extracted parameters for each of the detectors is presented in Table 1.

Table 1. Summary of detector parameters for each of three detectors.

Epilayer Thickness (µm)	Φ_B (eV)	n	N_{eff} (10^{14} cm^{-3})	Resolution (% FWHM)	L_d (µm)
50	1.43	1.30	1.61	2.0	16
150	1.55	1.56	1.59	0.78	10
250	1.46	1.14	1.74	0.63	9.2

3.3 Deep Level Transient Spectroscopy

DLTS is a powerful and sensitive tool which uses the peaks in the capacitance difference spectra to extract the properties of deep levels in the material. DLTS measurements were conducted on the three detectors from 200-790 K at a steady state bias of -5 V following a 1 ms trap filling pulse of 0 V. Immediately following the filling pulse, the saturated travel levels will start thermally emitting and be ejected from the depletion region causing the capacitance to decay to the steady state capacitance $C_0(V)$ given by,

$$C(t) = C_0(V) + \Delta C \exp(-e_n t) \tag{6}$$

where, ΔC is the change in capacitance while traps are completely occupied and e_n is the electron emission rate which is related the temperature by Eq. 7 [38].

$$e_n = \sigma_n \beta T^2 \exp\left(-\frac{E_a}{k_B T}\right). \tag{7}$$

Here, σ_n is the trap's electron capture cross-section, β is a constant related to the mean thermal velocity of electrons $\langle v_{th,n} \rangle$, and E_a is the thermal activation energy of the trap measured relative to the conduction band edge. Furthermore, the trap concentration can be determined from the ratio between ΔC and C_0 by the following,

$$N_t = 2\left(\frac{\Delta C}{C_0(V)}\right) N_{eff}. \tag{8}$$

The electron trapping lifetime τ_n is defined as the average time it takes for an electron traveling along some path to be collide with a trap center and be captured and thus can be defined as the mean free path L_t divided by the mean velocity of carriers. L_t for an individual trap is defined as $1/\sigma_n N_t$. For multiple traps all acting as recombination centers, the electrons can be trapped by any of the available trap centers and the mean free path becomes the reciprocal sum of the mean free paths for each of the individual traps. Thus, the electron trapping time can be represented as [19]

$$\frac{1}{\tau_n} = \langle v_{th,n} \rangle \sum_i N_{t,i}\, \sigma_{n,i}. \tag{9}$$

Hence, the larger the trap concentration and cross-section are, the shorter is the trapping time, which will adversely impact the resolution of the detector.

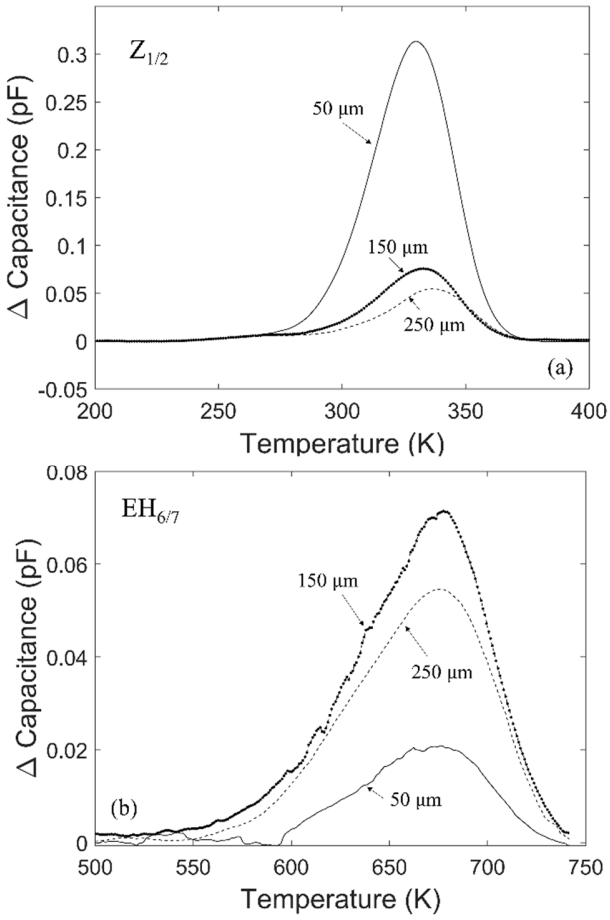

Figure 5. Deep level transient spectrums obtained using 0.5 ms initial delays and zoomed in on the $Z_{1/2}$ peak (a) and the spectra obtained using 10 ms initial delays zoomed in on $EH_{6/7}$ (b) for each of the three detectors.

Table 2. Summary of defect parameters extracted from the DLTS spectra of the three detectors.

Thickness (µm)	**$Z_{1/2}$**			**$EH_{6/7}$**		
	N_t (10^{11} cm^{-3})	σ_n (10^{-15} cm^2)	E_a (eV)	N_t (10^{11} cm^{-3})	σ_n (10^{-15} cm^2)	E_a (eV)
50	23	130	0.73	1.8	19	1.59
150	8.6	1.4	0.60	2.6	38	1.63
250	5.3	0.26	0.56	5.3	3.2	1.49

In as-grown 4H-SiC epitaxial layers, the two lifetime limiting defects that appear in all epilayers are $Z_{1/2}$ and $EH_{6/7}$—both of which are related to carbon vacancies [20, 25, 39-42]. Figs. 5(a) and (b) shows the

DLTS spectrum of the detectors zoomed in on the $Z_{1/2}$ and $EH_{6/7}$ peaks while the extracted activation energies, capture cross-sections, and trap concentrations are recorded in Table 2. The 50 µm detector had both the highest $Z_{1/2}$ capture cross-section and trap concentration at 1×10^{-13} cm^2 and 2.3×10^{12} cm^{-3}, respectively. While the trap concentration was only ~3 times higher than the 150 µm detector, its capture cross-section was two orders of magnitude higher explaining the huge performance jump between the two detectors. The 250 µm detector had both a lower $Z_{1/2}$ trap concentration and capture cross-section than the other two detectors. $EH_{6/7}$ had roughly the same order of magnitude concentrations for all three detectors although the 250 µm detector had a cross-section one order of magnitude lower.

4. Conclusions

4H-SiC epitaxial layers of thickness 50, 150, and 250 µm grown on low resistivity bulk 4H-SiC substrates were used as the semiconductor layer in Ni/n-4H-SiC Schottky radiation detectors. The three devices showed rectifying behavior confirming the existence of the Schottky barrier. The strongest rectification came from the detector fabricated on the 250 µm layer which had the ideality factor of closest to unity. Radiation detection measurements on the three detectors showed that the 250 µm detector had the best resolution of 0.63% FWHM compared to 0.78% and 2.0% for 150 and 50 µm, respectively. In semiconductor radiation detectors, the resolution is primarily limited by trapping from deep levels in epitaxial layers. To investigate the hole trapping properties, the drift-diffusion model was applied to the charge collected vs. applied bias characteristics which revealed that the worst resolution detector had the least minority carrier trapping, implying that the device performance was not limited by holes. The electron trapping parameters were determined from the capacitance mode DLTS spectra over the temperate range 200-790 K which revealed two lifetime limiting defects $Z_{1/2}$ and $EH_{6/7}$. By relating the product of the trap capture cross-section and concentration to the electron trapping lifetime, it was found that the best resolution detector fabricated on 250 µm epilayers had both the lowest $Z_{1/2}$ concentration and cross-section product.

Acknowledgment

This work was supported by the DOE Office of Nuclear Energy's Nuclear Energy University Program (NEUP), Grant No. DE-AC07-051D14517 & DE-NE0008662. The work was also supported in part by the Advanced Support Program for Innovative Research Excellence-I &-II (ASPIRE-I & ASPIRE-II), Grant No. 15530-E404 & 155312-N1600 of the University of South Carolina (UofSC), Columbia, USA.

References:

[1] K.C. Mandal, J.W. Kleppinger, S.K. Chaudhuri, Advances in high-resolution radiation detection using 4H-SiC epitaxial layer devices, Micromachines, 11 (2020) 254. https://doi.org/10.3390/mi11030254.
[2] D. Puglisi, G. Bertuccio, Silicon carbide microstrip radiation detectors, Micromachines, 10 (2019) 835. https://doi.org/10.3390/mi10120835.
[3] F. Nava, G. Bertuccio, A. Cavallini, E. Vittone, Silicon carbide and its use as a radiation detector material, Meas. Sci. Technol. 19 (2008) 102001. http://dx.doi.org/10.1088/0957-0233/19/10/102001.
[4] J.W. Kleppinger, S.K. Chaudhuri, O. Karadavut, K.C. Mandal, Defect characterization and charge transport measurements in high-resolution Ni/n-4H-SiC Schottky barrier radiation detectors fabricated on 250 µm epitaxial layers, J. Appl. Phys. 129 (2021) 244501. https://doi.org/10.1063/5.0049218.
[5] J.W. Kleppinger, S.K. Chaudhuri, O. Karadavut, K.C. Mandal, Role of deep levels and barrier height lowering in current-flow mechanism in 150 µm thick epitaxial n-type 4H–SiC Schottky barrier radiation detectors, Appl. Phys. Lett. 119 (2021) 063502. https://doi.org/10.1063/5.0064036.
[6] F.H. Ruddy, A.R. Dulloo, J.G. Seidel, M.K. Das, R. Sei-Hyung, A.K. Agarwal, The fast neutron response of 4H silicon carbide semiconductor radiation detectors, IEEE Trans. Nucl. Sci. 53 (2006) 1666-1670. https://doi.org/10.1109/TNS.2006.875151.

[7] F. Zhao, M.M. Islam, C.-F. Huang, Photoelectrochemical etching to fabricate single-crystal SiC MEMS for harsh environments, Mater. Lett. 65 (2011) 409-412. https://doi.org/10.1016/j.matlet.2010.10.034.
[8] C.S. Bodie, G. Lioliou, A.M. Barnet, 2021. Hard X-ray and γ-ray spectroscopy at high tempratures using a COTS SiC photdiode. Nucl. Instrum. Meth. Phys. Res. A. 985, 164663. https://doi.org/10.1016/j.nima.2020.164663.
[9] P.G. Neudeck, D.J. Spry, M.J. Krasowski, N.F. Prokop, L. Chen, Demonstration of 4H-SiC JFET digital ICs across 1000 °C temperature range without change to input voltages, Mater. Sci. Forum, 963 (2019) 813-817. https://doi.org/10.4028/www.scientific.net/MSF.963.813.
[10] G. Lucas, L. Pizzagalli, Comparison of threshold displacement energies in β-SiC determined by classical potentials and ab initio calculations, Nucl. Instrum. Method Phys. Res. B, 229 (2005) 359-366. https://doi.org/10.1016/j.nimb.2004.12.119.
[11] G. Bertuccio, D. Puglisi, L. Torrisi, C. Lanzieri, Silicon carbide detector for laser-generated plasma radiation, Appl. Surf. Sci. 272 (2013) 128-131. https://doi.org/10.1016/j.apsusc.2012.03.183.
[12] S.M. Griffin, Y. Hochberg, K. Inzani, N. Kurinsky, T. Lin, T.C. Yu, SiC detectors for sub-GeV dark matter, Phys. Rev. D, 103 (2020) 075002. https://doi.org/10.1103/PhysRevD.103.075002.
[13] Z. Wang, D. Zhou, W. Xu, D. Pan, F. Ren, D. Chen, R. Zhang, Y. Zheng, H. Lu, High-performance 4H-SiC Schottky photodiode with semitransparent grid-electrode for EUV detection, IEEE Photon. Technol. Lett. 32 (2020) 791-794. https://doi.org/10.1109/LPT.2020.2996308.
[14] K.C. Mandal, R.M. Krishna, P.G. Muzykov, S. Das, T.S. Sudarshan, Characterization of semi-insulating 4H silicon carbide for radiation detectors, IEEE Trans. Nucl. Sci. 58 (2011) 1992-1999. https://doi.org/10.1109/TNS.2011.2152857.
[15] W. Cunningham, A. Gouldwell, G. Lamb, J. Scott, K. Mathieson, P. Roy, R. Bates, P. Thornton, K.M. Smith, R. Cusco, M. Glaser, M. Rahman, Performance of bulk SiC radiation detectors, 3rd International Workshop on Radiation Imaging Detectors, 487 (2002) 33-39. https://doi.org/10.1016/S0168-9002(02)00941-5.
[16] G. Bertuccio, D. Puglisi, A. Pullia, C. Lanzieri, X-γ ray spectroscopy with semi-insulating 4H-silicon carbide, IEEE Trans. Nucl. Sci. 60 (2013) 1436-1441. https://doi.org/10.1109/TNS.2013.2252019.
[17] S.O. Kasap, M.Z. Kabir, K.O. Ramaswami, R.E. Johanson, R.J. Curry, 2020. Charge collection efficiency in the presence of non-uniform carrier drift mobilities and lifetimes in photoconductive detectors. J. Appl. Phys. 128, 124501. https://doi.org/10.1063/5.0017521.
[18] M. Zahangir Kabir, E. V. Emelianova, V. I. Arkhipov, M. Yunus, S. O. Kasap, G. Adriaenssens, 2006. The effects of large signals on charge collection in radiation detectors: Application to amorphous selenium detectors. J. Appl. Phys. 99, 124501. https://doi.org/10.1063/1.2206096.
[19] J. Erlekampf, M. Rommel, K. Rosshirt-Lilla, B. Kallinger, P. Berwian, J. Friedrich, T. Erlbacher, Lifetime limiting defects in 4H-SiC epitaxial layers: The influence of substrate originated defects, J. Cryst. Growth, 560-561 (2021) 126033. https://doi.org/10.1016/j.jcrysgro.2021.126033.
[20] T. Kimoto, K. Danno, J. Suda, Lifetime-killing defects in 4H-SiC epilayers and lifetime control by low-energy electron irradiation, phys. status solidi (b), 245 (2008) 1327-1336. https://doi.org/10.1002/pssb.200844076.
[21] S. Ha, P. Mieszkowski, M. Skowronski, L.B. Rowland, Dislocation conversion in 4H silicon carbide epitaxy, J. Cryst. Growth, 244 (2002) 257-266. https://doi.org/10.1016/S0022-0248(02)01706-2.
[22] T. Ohno, H. Yamaguchi, S. Kuroda, K. Kojima, T. Suzuki, K. Arai, Influence of growth conditions on basal plane dislocation in 4H-SiC epitaxial layer, J. Cryst. Growth, 271 (2004) 1-7. https://doi.org/10.1016/j.jcrysgro.2004.04.044.
[23] H. Song, T.S. Sudarshan, Basal plane dislocation conversion near the epilayer/substrate interface in epitaxial growth of 4° off-axis 4H–SiC, J. Cryst. Growth, 371 (2013) 94-101. https://doi.org/10.1016/j.jcrysgro.2013.02.011.
[24] H. Fujiwara, K. Danno, T. Kimoto, T. Tojo, H. Matsunami, Effects of C/Si ratio in fast epitaxial growth of 4H–SiC(0001) by vertical hot-wall chemical vapor deposition, J. Cryst. Growth, 281 (2005) 370-376. https://doi.org/10.1016/j.jcrysgro.2005.03.093.

[25] J. Zhang, L. Storasta, P.J. Bergman, P.J. Son, J. E., Electrically active defects in n-type 4H–silicon carbide grown in a vertical hot-wall reactor, J. Appl. Phys. 4708-4714 (2003) 93. https://doi.org/10.1063/1.1543240.
[26] M.A. Mannan, S.K. Chaudhuri, K.V. Nguyen, K.C. Mandal, Effect of $Z_{1/2}$, EH_5, and Ci1 deep defects on the performance of n-type 4H-SiC epitaxial layers Schottky detectors: Alpha spectroscopy and deep level transient spectroscopy studies, J. Appl. Phys. 115 (2014) 224504. https://doi.org/10.1063/1.4883317.
[27] K.C. Mandal, S.K. Chaudhuri, K.V. Nguyen, M.A. Mannan, Correlation of deep levels with detector performance in 4H-SiC epitaxial schottky barrier alpha detectors, IEEE Trans. Nucl. Sci. 61 (2014) 2338-2344. https://doi.org/10.1109/TNS.2014.2335736.
[28] S.K. Chaudhuri, J.W. Kleppinger, K.C. Mandal, Radiation detection using fully depleted 50 μm thick Ni/n-4H-SiC epitaxial layer Schottky diodes with ultra-low concentration of $Z_{1/2}$ and $EH_{6/7}$ deep defects, J. Appl. Phys. 128 (2020) 114501. https://doi.org/10.1063/5.0021403.
[29] W. Kern, The evolution of silicon wafer cleaning technology, J. Eletrochem. Soc. 137 (1990) 1887-1892. http://doi.org/10.1149/1.2086825.
[30] E.H. Rhoderick, Metal-semiconductor contacts, IEE Proc. I - Solid-State Electron Devices, 129 (1982) 1. https://doi.org/10.1049/ip-i-1.1982.0001.
[31] S.M. Sze, K.K. Ng, Physics of Semiconductor Devices, John Wiley & Sons, New York, 2007.
[32] B.J. Skromme, E. Luckowski, K. Moore, M. Bhatnagar, C.E. Weitzel, T. Gehoski, D. Ganser, Electrical characteristics of schottky barriers on 4H-SiC: The effects of barrier height nonuniformity, J. Electron. Mater. 29 (2000) 376-383. https://doi.org/10.1007/s11664-000-0081-9.
[33] R.T. Tung, Electron transport at metal-semiconductor interfaces: General theory, Phys. Rev. B, 45 (1992) 13509-13523. https://doi.org/10.1103/PhysRevB.45.13509.
[34] F. Triendl, G. Pfusterschmied, G. Pobegen, J.P. Konrath, U. Schmid, Theoretical and experimental investigations of barrier height inhomogeneities in poly-Si/4H-SiC heterojunction diodes, Semicond. Sci. Technol. 35 (2020) 115011. http://dx.doi.org/10.1088/1361-6641/abae8d.
[35] K. Hecht, Zum mechanismus des lichtelektrischen primärstromes in isolierenden kristallen, 77 (1932) 235-245. https://doi.org/10.1007/BF01338917.
[36] S.K. Chaudhuri, K.J. Zavalla, K.C. Mandal, High resolution alpha particle detection using 4H–SiC epitaxial layers: fabrication, characterization, and noise analysis, Nucl. Instrum. Method Phys. Res. A, 728 (2013) 97-101. https://doi.org/10.1016/j.nima.2013.06.076.
[37] C. Manfredotti, F. Fizzotti, A. Lo Giudice, C. Paolini, E. Vittone, F. Nava, Investigation of 4H–SiC Schottky diodes by ion beam induced charge (IBIC) technique, Appl. Surf. Sci. 184 (2001) 448-454. https://doi.org/10.1016/S0169-4332(01)00533-5.
[38] D.V. Lang, Deep-level transient spectroscopy: A new method to characterize traps in semiconductors, J. Appl. Phys. 45 (1974) 3023-3032. https://doi.org/10.1063/1.1663719.
[39] K. Danno, T. Kimoto, H. Matsunami, Midgap levels in both n- and p-type 4H–SiC epilayers investigated by deep level transient spectroscopy, Appl. Phys. Lett. 86 (2005) 122104. https://doi.org/10.1063/1.1886904.
[40] G. Alfieri, T. Kimoto, Resolving the $EH_{6/7}$ level in 4H-SiC by laplace-transform deep level transient spectroscopy, Appl. Phys. Lett. 102 (2013) 152108. https://doi.org/10.1063/1.4802248.
[41] L. Gordon, A. Janotti, C.G. Van de Walle, Defects as qubits in 3C- and 4H-SiC, Phys. Rev. B, 92 (2015) 045208. https://doi.org/10.1103/PhysRevB.92.045208.
[42] T. Kobayashi, K. Harada, Y. Kumagai, F. Oba, Y.-i. Matsushita, Native point defects and carbon clusters in 4H-SiC: A hybrid functional study, J. Appl. Phys. 125 (2019) 125701. https://doi.org/10.1063/1.5089174.